

# **Evolution of topological surface states of thin HgTe-films with film thickness**

**Bachelor thesis**

Verfasst von Tamara Szecsey

March 20, 2017



Universität Regensburg

Fakultät Physik

Im Bereich theoretischer Festkörperphysik

Unter der Betreuung von

Prof. Dr. Ferdinand Evers

und

Maria Camarasa-Gomez

Ich habe die Arbeit selbständig verfasst, keine anderen als die angegebenen Quellen und Hilfsmittel benutzt und bisher keiner anderen Prüfungsbehörde vorgelegt. Außerdem bestätige ich hiermit, dass die vorgelegten Druckexemplare und die vorgelegte elektronische Version der Arbeit identisch sind, dass ich über wissenschaftlich korrektes Arbeiten und Zitieren aufgeklärt wurde und dass ich von den in § 24 Abs. 5 vorgesehenen Rechtsfolgen Kenntnis habe.

# Contents

<b>1</b>	<b>Introduction</b>	<b>1</b>
<b>2</b>	<b>Theory</b>	<b>2</b>
2.1	Topological insulators . . . . .	2
2.2	Description of a crystal structure . . . . .	3
2.3	Crystal surfaces. . . . .	4
2.3.1	The zinc blende crystal and its (001) cleavage . . . . .	4
2.3.2	Reciprocal lattice and first Brillouin zone. . . . .	6
2.3.3	Surface modeling . . . . .	7
2.4	Basics of Density Functional Theory . . . . .	9
2.4.1	The ground-state functional . . . . .	9
2.4.2	Approximations for the exchange-correlation functional . . . . .	11
2.5	Spin-orbit coupling . . . . .	11
2.5.1	Spin-orbit coupling in Schrödinger equation . . . . .	11
2.5.2	SOC impact on band structure . . . . .	13
<b>3</b>	<b>Results</b>	<b>15</b>
3.1	Input for FHI-aims . . . . .	15
3.2	The lattice constant and the k-grid . . . . .	16
3.3	The bulk band structure in the first 3D Brillouin zone . . . . .	18
3.4	Projected bulk band structure . . . . .	19
<b>4</b>	<b>Interpretation of the results</b>	<b>25</b>
4.1	k-grid study . . . . .	25
4.2	Lattice constant study . . . . .	25
4.3	Bulk band structure . . . . .	25
4.4	PBBS and the band structure of the slabs . . . . .	25
<b>5</b>	<b>Conclusion</b>	<b>27</b>

# 1 Introduction

During the last ten years, topological insulators were the most examined topic in condensed matter physics. These materials are insulating in their interior, also known as the bulk, but possess conducting surface states. This quality makes it very exotic and attractive for potential applications. Therefore big effort was made in order to find materials of this kind. One of these is HgTe for which we studied the evolution of topological surface states in this thesis [11].

More explicit, we concentrate us on the topological surface states in the surface growing direction (001). We approach this problem by performing ab-initio calculations, in detail, we used density functional theory (DFT) through the commercial package FHI-aims.

By combining the supercell approach and the projected bulk band structure we observe how sensitive the energy band structure, as well as the surface states react on different thicknesses and terminations of the slabs. Additionally we thus will see the evolution of the surface states in this material regarding the (001) plane.

This thesis is divided into five parts: In part one we give an introduction of the main topic. In part two we give an explanation of the theoretical background including the concept of topological insulators, the basic principles for numeric modeling of surfaces by applying density functional theory and the origins of spin-orbit interaction in solid state matter. In part three of this thesis we present the results of our calculations for the slab band structure of HgTe with various thicknesses and in cases of ideal and passivated surfaces. In part four we interpret those results. And finally in part five we close this thesis by conclusions.

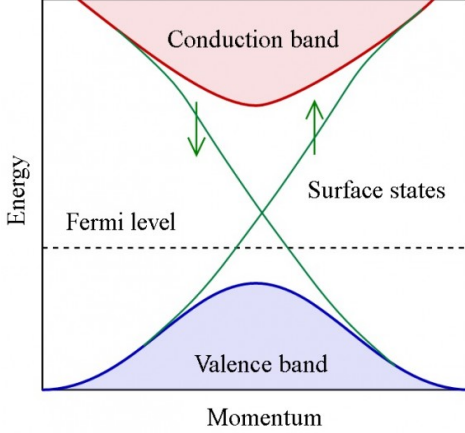


**Figure 1.** Sketch of band structure of a topological insulator near the Fermi level (dashed lines). In blue: valence band, in red: conduction band, in green: the surface states with nearly linear dispersion close to the Fermi level. Each branch of the Dirac cone have opposite spin polarization in respect to the other branch. (Picture from [1])

## 2 Theory

### 2.1 Topological insulators

Originally, materials were named conductors if by applying an electric field or an isolator small electric currents start to flow as a reaction to the external field.

But 2005 Kane and Mele [9] discovered that apart from the insulators, the conductors and the semi-conductors, there is an other class of material: the so-called topological insulator, which acts like an insulator in the inner part (bulk) but is conductive at the surface. Additionally the surface states of these topological insulators are special in comparison with normal surfaces since they are symmetry protected by time-reversal symmetry and because of their band structure.

From a practical point of view topological insulators arise by combination of spin-orbit interactions, which itself provide spin-momentum locking and band inversion, and closed energy bands. Because of the spin-momentum locking, backscattering is not possible for surface states as long as time-reversal symmetry is preserved. The reason is, that the spin can not change while the momentum doesn't. The band inversion is the origin for the characteristic Dirac cones of the surface states which lie between the band gap. Note that the surface states cannot be removed by modification. For example by passivation or disorder, as long as time-reversal symmetry is preserved.

In 2D a topological insulator possesses 1D edge channels which are counter propagating and spin polarized [10]. They are known as quantum spin Hall edge states and were first predicted in graphene [10] but later were found in HgTe quantum wells [7].

Quantum wells have non-trivial topological surface states under a certain critical thickness but become trivial insulators as soon as they pass this critical thickness.

The prediction was closely followed by the generalization of the concept of topological

insulators on to 3D. In this dimension there are two different kinds of topological insulators which are defined by the band structure characteristics: There are strong topological insulators which have an odd number of Dirac cones in the bulk band structure and there are weak ones with an even number of those Dirac cones.

HgTe, which is the material we consider in this thesis, is also a 3D topological insulator under certain circumstances. In general it is a semi metal, but under applied strain its  $\Gamma_6$  and  $\Gamma_8$  bands close up at the Fermi level [8]. This was confirmed by experimental ARPRES and transport measurements.

An interesting question is what happens to the band structure and the topological properties by applying strains in one direction. This question will be partly answered in the following sections.

## 2.2 Description of a crystal structure

A crystal structure describes the arrangement of atoms in a crystalline material. The atoms out of which a crystal is made, maintain a symmetric pattern repeating itself into the three spatial dimensions.

For this reason, to describe the crystal structure, one needs a basis, which can start at any atom  $i$  in the lattice, in order to form a unit cell. For a three dimensional crystal, we need a three dimensional lattice and to describe the crystal lattice we introduce three primitive translation vectors  $\mathbf{a}_1, \mathbf{a}_2$  and  $\mathbf{a}_3$ . These vectors indicate the directions where to the atom  $i$  of the crystal, which holds the coordinates  $x_i, y_i$  and  $z_i$ , must be replicated in order to compose the whole crystalline structure. The crystal translation vector  $\mathbf{R}_i$  is then defined as

$$\mathbf{R}_i = x_i \mathbf{a}_1 + y_i \mathbf{a}_2 + z_i \mathbf{a}_3 \quad (2.1)$$

There are different ways to choose the basis set for the unit cells, some possible choices for a two dimensional lattice are illustrated in figure 2. In this figure one can also see some unit cells, shown in grey areas, that, with the exception of 4, are primitive unit cells.

A primitive cell is a unit cell which includes the smallest possible number of atoms and possesses the minimum volume whose lattice vectors describe the crystal lattice. Its basis vectors do not include atoms like they are in cell 4 in figure 2, which has, was we can see, twice the volume of cell example number 1. There are many ways of choosing the basis, the parallelograms 1, 2 and 3 are examples of primitive cells. The smallest primitive cell is the Wigner-Seitz cell and is defined as the unit cell, which contains one single atom that is placed at its center. In 2D it can be constructed by linking the basis atom with all next neighbors by a line, put a straight line at the middle of each line, and then the space around the basis atom is the Wigner-Seitz cell.

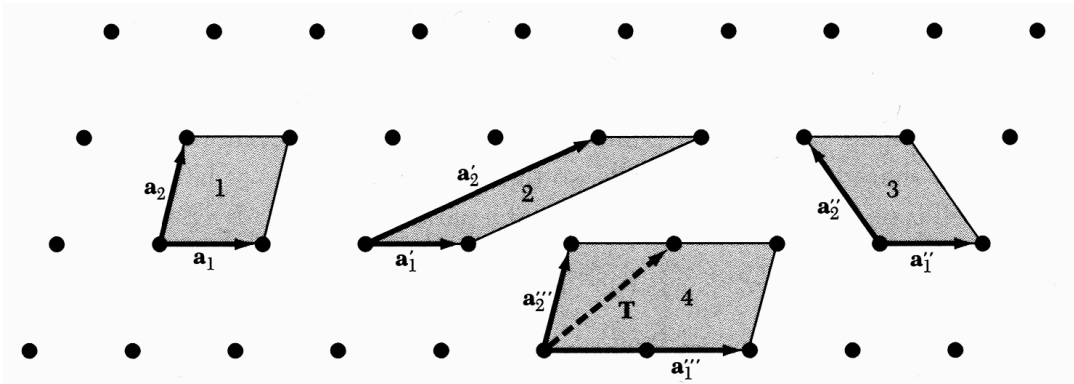


**Figure 2.** Some two dimensional unit cells with different basis vectors. The cells 1,2 and 3 are primitive unit cells, but 4 is not because its volume is twice as big as, for example, the parallelogram number 1. For a primitive cell it must be verified that the volume is as small as possible in order to reproduce the lattice when repeated in space in all directions considered. (Picture from[13])

## 2.3 Crystal surfaces.

### 2.3.1 The zinc blende crystal and its (001) cleavage

Now we introduce the concept of Bravais lattices. A Bravais lattice is defined by an infinite number of discrete points which are arranged in a translational symmetric way. It is described by a vector  $\mathbf{R}$  given by (2.1), whereat the points are generated by integer translations. Each point can be connected to a basis of one or more atoms.

In three dimensional space, there are 14 different types of Bravais lattices. In this thesis we work with the so called face-centered cubic (fcc) lattice with a basis composed of two different species of atoms. This lattice is also known as zinc-blende structure which is similar to the diamond structure whose basis contains two identical basis atoms at  $(0, 0, 0)$  and  $(\frac{a}{4}, \frac{a}{4}, \frac{a}{4})$ . Note that this structure can be understood as two fcc lattices which are shifted in respect to each other. The coordinates of the atoms and the primitive basis vectors can be seen in figure 3 and a picture of the zinc-blende structure is shown in figure 5.

Crystals are grown plane by plane in different directions. Those planes can be identified by the so called miller indices  $(hkl)$ . The integers  $h$ ,  $k$  and  $l$  are obtained by multiplying each basis vector with a number, so that it touches the plane, inverting these numbers  $x$ ,  $y$  and  $z$  in respect to multiplication, in other words, writing them in a fractions denominator, whereby these fractions are in the same ratio as the miller indices, and finally expand the fractions until they are integers indivisible by another integer. The connection between the miller indices and the numbers  $x$ ,  $y$  and  $z$  is

$$h : k : l = \frac{1}{x} : \frac{1}{y} : \frac{1}{z} \quad (2.2)$$

Some examples can be seen in figure 4.

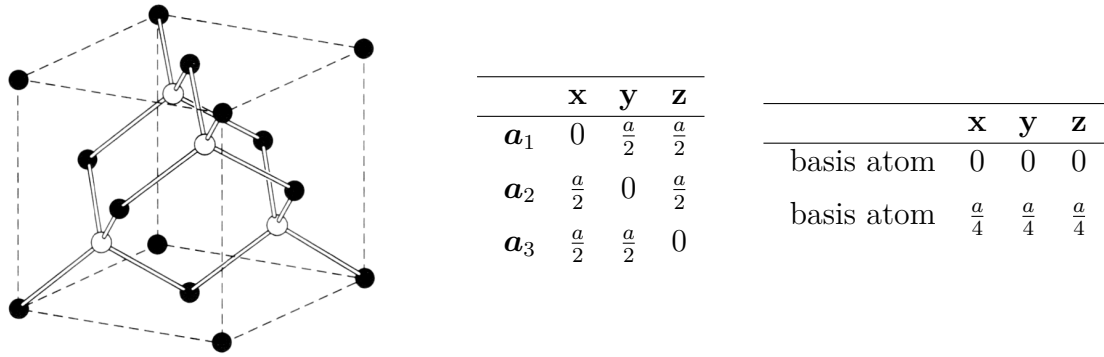


**Figure 3.** This is the cubic diamond lattice on the left (Picture from[13]). In the middle there are the basis lattice vectors of the primitive unit cell for a diamond crystal, and on the right there are the basis atoms for fcc and diamond.

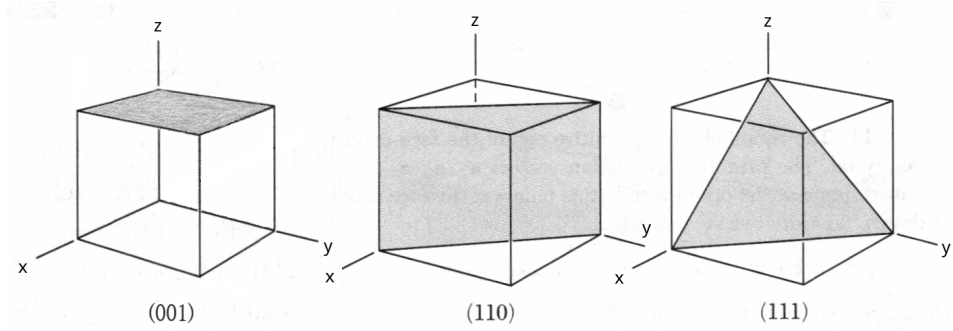


**Figure 4.** Important planes in cubic crystals with their indices. At the left, there is the (001) which is analyzed for HgTe zinc blende structure in this thesis. (Picture from[13])

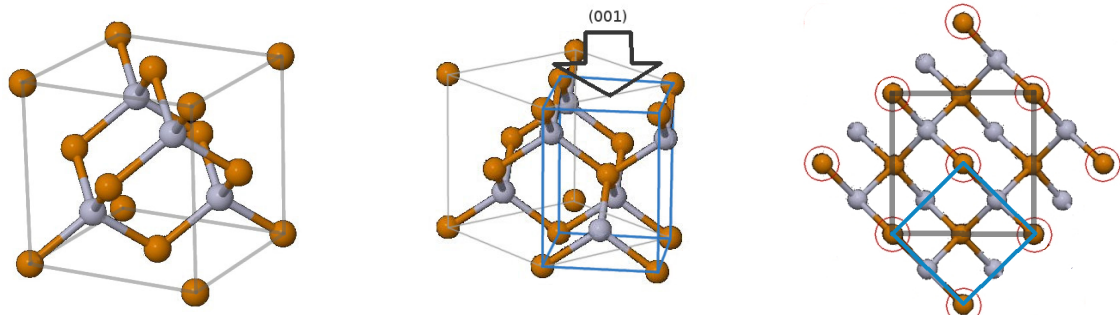


**Figure 5.** Left: zinc blende structure, two different kinds of atoms are labeled as Te (orange) and Hg (grey), note that this is not a primitive unit cell. Middle: rotation of basis by  $45^\circ$ , so that the new unit cell is the blue cuboid. Right: the top view. The red circles mark the atoms at the top, the blue lines are the small cell with length  $\frac{a}{\sqrt{2}}$ . The grey large square represents the (001) plane of the old unit cell.

In this thesis we will focus on the study of mercury telluride which is a crystal with two basis atoms Hg and Te, arranged in a zinc-blende structure. In order to perform the calculations, we are focusing on HgTe at the diamond (001) cleavage, which is the top plane illustrated in figure 4. It is convention not to use the unit cell in the left of figure 5, but to rotate the basis by 45°, like on the right. This has the advantage, that the unit cell contains less atoms.

The lattice vectors for diamond(001) are given by

$$\mathbf{a}_1 = \frac{a}{\sqrt{2}}\hat{\mathbf{x}}; \quad \mathbf{a}_2 = \frac{a}{\sqrt{2}}\hat{\mathbf{y}}; \quad \mathbf{a}_3 = a\hat{\mathbf{z}} \quad (2.3)$$

where  $a$  is the lattice constant of the crystal [14] illustrated in the to the right in figure 5. In our case the basis atoms are at

	<b>x</b>	<b>y</b>	<b>z</b>
atomic species 1	0	0	0
atomic species 2	$\frac{a}{2\sqrt{2}}$	0	$\frac{a}{4}$
atomic species 1	$\frac{a}{2\sqrt{2}}$	$\frac{a}{2\sqrt{2}}$	$\frac{a}{2}$
atomic species 2	0	$\frac{a}{2\sqrt{2}}$	$\frac{3a}{4}$

### 2.3.2 Reciprocal lattice and first Brillouin zone.

The reciprocal lattice is defined as the Fourier transform of the direct Bravais lattice in real space. This transformation is mathematically equivalent to

$$e^{i\mathbf{K}\cdot\mathbf{R}} = 1. \quad (2.4)$$

where  $\mathbf{K}$  is the set of wave vectors in reciprocal space and  $\mathbf{R}$  is defined as in Eq. 2.1. Consequently, every direct lattice has a corresponding reciprocal lattice which in addition, is a Bravais lattice too, since the Fourier transform acts within a group of discrete symmetries. The primitive translation vectors of the reciprocal lattice can be obtained from Eq. 2.4 and their basis vectors are in three dimensional space related to the direct lattice vectors as

$$\mathbf{b}_1 = \frac{2\pi}{V}(\mathbf{a}_2 \times \mathbf{a}_3); \quad \mathbf{b}_2 = \frac{2\pi}{V}(\mathbf{a}_3 \times \mathbf{a}_1); \quad \mathbf{b}_3 = \frac{2\pi}{V}(\mathbf{a}_1 \times \mathbf{a}_2) \quad (2.5)$$

with  $V = \mathbf{a}_1 \cdot \mathbf{a}_2 \times \mathbf{a}_3$  being the volume of the primitive unit cell in real space.

The primitive Wigner-Seitz cell in the reciprocal space is called the first Brillouin zone. The principle of constructing the first Brillouin zone is the same as for the earlier described Wigner-Seitz cells construction. The points, who stand out as high-symmetry points of the Brillouin zone, are marked by letters like K, L, U etc. The center of the Brillouin zone which happens to also be the origin of the Fourier space, is marked with the greek letter  $\Gamma$ . The first Brillouin zone of the fcc and diamond crystal is shown in figure 6.

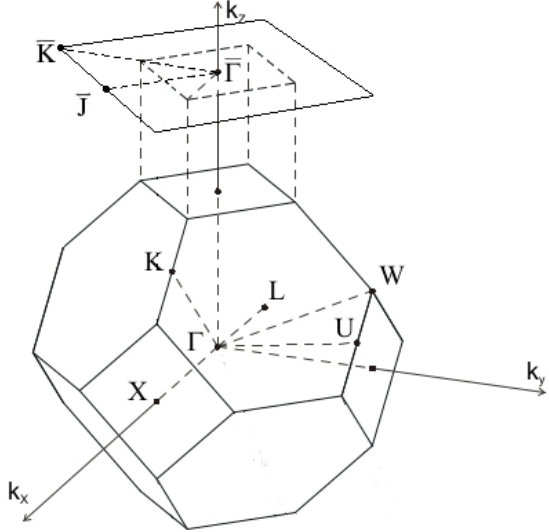


**Figure 6.** First Brillouin zone of a fcc and diamond lattice. The plane at the top shows the 3D Brillouin zone projected in (001) direction, which is also defined by the vector  $\mathbf{b}_3$ . This corresponds to the first Brillouin zone in the 2D lattice. The high symmetry point are marked with latin letters, whereby the ones in the two dimensional Brillouin zone additionally have a bar and the point of origin is marked with a  $\Gamma$ , a bar is added for the one in the 2D Brillouin zone. (Picture originally from[16])

The bulk band structure (see figure 11), which gives the total energy in respect to the momentum, can now be seen as a one dimensional representation of a certain path which follows the high-symmetry points in the first Brillouin zone.

For the 2D periodic crystal slab, which grows in (001) direction, a two dimensional path can be taken along the high-symmetry points  $\bar{\Gamma}$ ,  $\bar{J}$  and  $\bar{K}$ . These points can be represented in terms of the reciprocal vectors  $\mathbf{b}_1$  and  $\mathbf{b}_2$ :

$$\bar{\Gamma} = 0; \quad \bar{J} = \frac{1}{2}\mathbf{b}_1; \quad \bar{K} = \frac{1}{2}\mathbf{b}_1 + \frac{1}{2}\mathbf{b}_2 \quad (2.6)$$

Therefore the 2D Brillouin zone, which corresponds to the slab, is like the projection of the 3D Brillouin zone into a plane which is defined by the vector  $\mathbf{b}_3$ .

### 2.3.3 Surface modeling

The main goal of this thesis is to simulate the evolution of the topological surface states of HgTe. Therefore we first need to introduce the concept of surfaces and then simulate the (001) surface for an ideal slab.

The bulk is a model of a crystal which does not consider surfaces. For us, the most important difference are the boundary conditions. The bulk has periodic boundary conditions in all three spacial directions, but the slab, has these in just two directions,

in particular the x and y direction. Thus  $k_z$  is no longer a good quantum number. How this direction is simulated is explained in the following paragraphs.

**Terminations** While simulating the slab, one must consider two surfaces which are both terminated with atoms. Thereby it is very difficult to find a way to prevent interactions between the surfaces. In a real simulation this is done by passivating one surface for example by adding hydrogen atoms, in order to get a neutral surface. These hydrogens saturate the dangling bonds, the unsatisfied valences on immobilized atoms.

During this work, we study diverse possible terminations. On the one hand it is the symmetrical case with Hg-Hg and Te-Te as termination on both surface, on the other hand, we regard the antisymmetrical case with Te-Hg termination, whereby also both versions, with and without passivation with hydrogen, are studied.

**Number of layers** As mentioned before, the main goal of this thesis is the investigation of the topological surface states' evolution by adding layers in one growth direction. Discussing the number of layers is therefore essential. The termination defines whether the number of layers is even or odd. For the slabs with same atom termination the number of layers is odd and for the ones with different atom termination it is even.

For each one we took 3 different numbers of layers in order to simulate the growth of a mercury telluride crystal in the (001) plane, observing at which thickness the surface states presents characteristics of those of a topological insulator. One layer is defined as one of five layers in the crystal unit cell in figure 5, in other words, for your coordination choice all atoms with the same z-component are in the same layer.

**The Supercell Approach** For simulating the surface structure of a crystal, the so-called supercell approach might be useful. The concept is rather simple. First one constructs the unit cell for the slabs, which will be duplicated infinite times in all directions. Since  $k_z$  is a bad quantum number, the repetition in z-direction presents a problem. But FHI-aims can only solve the Schrödinger equation with periodic boundary condition applied in all three directions. This means, that in x and y direction, the lattice is repeated into infinity but, also the the

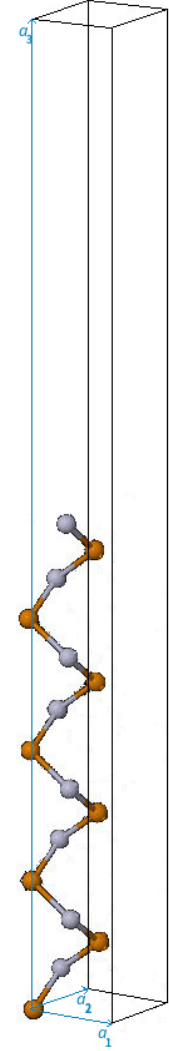


**Figure 7.** Supercell with 16 layers and additional space at the top, representing the vacuum. Basis vectors  $\mathbf{a}_1$ ,  $\mathbf{a}_2$  like in eq. 2.3,  $\mathbf{a}_3$  with additional vacuum thickness.

slabs from an infinite stack into the z-direction. To prevent interactions between the surfaces, we add a sufficiently large vacuum slab to the supercell which makes sure that the slabs can be regarded as isolated. A supercell of 16 layers of HgTe is shown in figure 7.

## 2.4 Basics of Density Functional Theory

The density functional theory (DFT) is a computational method in quantum mechanics used for analyzing the ground state properties of physical systems. Ab-initio stands for calculations which are performed only by using fundamental laws of physics like the Schrödinger equation for quantum mechanical problems. At the same time, no approximations are taken whereby symmetries are still included. Consequently, one usually needs notable large computational resources. The DFT was first introduced by W.Kohn et al. [6]. Thereby it was found that the ground-state energy of a quantum mechanical system can be represented by the density functional. This simplifies the many-body problem down to a self-consistent one-body problem.

In the following most equations were adapted from [12]

### 2.4.1 The ground-state functional

Let us consider a system containing  $N$  electrons with Hamiltonian  $H_e$  that contains three parts: kinetic energy  $T$ , external potential  $V_{ext}$ , which describes the interaction between the electrons and a fixed nuclei background, and the two-body electron-electron interaction known as the Coulomb potential  $V_{ee}$ .

$$H_e = T + V_{ee} + V_{ext} = \sum_i \frac{\mathbf{p}_i^2}{2m} + \frac{1}{2} \sum_{i \neq j} \frac{e^2}{|\mathbf{r}_i - \mathbf{r}_j|} + \sum_i v_{ext}(\mathbf{r}_i) \quad (2.7)$$

$$\text{with } v_{ext}(\mathbf{r}) = V_{\text{nucl}}(\mathbf{r}) = - \sum_I \frac{z_I e^2}{|\mathbf{r} - \mathbf{R}_I|} \quad (2.8)$$

where  $e$  is the elementary charge. The external potential  $V_{ext}$  contains the interaction between each proton  $I$  in the nuclei whereby  $z_I$  is the number of all protons in the nuclei, and each electron  $i$ ,  $v_{ext}(\mathbf{r})$  is therefore the external potential for a single electron in the potential background of a nuclei.

If  $\Psi_G(\mathbf{r}_1, \dots, \mathbf{r}_N)$  is the wave function of the ground state in the many body Schrödinger equation

$$H_e \Psi_G = E_G \Psi_G \quad (2.9)$$

then it can be shown, that the one-body ground states density, which is defined as

$$\rho(\mathbf{r}) = \langle \Psi_G(\mathbf{r}_1, \dots, \mathbf{r}_N) | \sum_i \delta(\mathbf{r} - \mathbf{r}_i) | \Psi_G(\mathbf{r}_1, \dots, \mathbf{r}_N) \rangle \quad (2.10)$$

can be uniquely converted into the external Potential  $V_{ext}(\mathbf{r})$  and vice versa. In other words, for one given  $V_{ext}(\mathbf{r})$  there exists specifically one  $\rho(\mathbf{r})$ . This is known as one of the Hohenberg-Kohn theorems [12].

The second Hohenberg-Kohn theorem says that the ground state energy can be expressed in a density functional. That functional is called the Hohenberg-Kohn energy functional ([12] p.133) and reads

$$E^{\text{HK}}[\rho(\mathbf{r}); v_{\text{ext}}(\mathbf{r})] = T[\rho(\mathbf{r})] + V_{\text{ee}}[\rho(\mathbf{r})] + \int v_{\text{ext}}(\mathbf{r})\rho(\mathbf{r})d\mathbf{r} \quad (2.11)$$

This means now the ground-state energy of a many-body problem can be disposed immediately if the density is known.

By rearranging the functional above, we define the so-called exchange-correlation functional  $E_{xc}[\rho]$ :

$$E_{xc}[\rho] = T[\rho] - T_0[\rho] + V_{\text{ee}}[\rho] - V_{\text{H}}[\rho] \quad (2.12)$$

so that equation (2.11) is now

$$E^{\text{HK}}[\rho(\mathbf{r}); v_{\text{ext}}(\mathbf{r})] = T_0[\rho] + V^{\text{HK}}(\mathbf{r}) \quad (2.13)$$

with the kinetic energy of a system with non-interacting electrons:

$$T_0[\rho] = \sum_i \langle \phi_i(\mathbf{r}) | -\frac{\hbar^2 \nabla^2}{2m} | \phi_i(\mathbf{r}) \rangle \quad (2.14)$$

and the Hohenberg-Kohn potential

$$V^{\text{HK}}(\mathbf{r}) = V_{\text{H}}[\rho] + \int v_{\text{ext}}(\mathbf{r})\rho(\mathbf{r})d\mathbf{r} + E_{xc}[\rho] \quad (2.15)$$

with the Hartree potential which is defined as

$$V_{\text{H}}[\rho] = \frac{1}{2} \sum_{i,j} \langle \phi_i \phi_j | \frac{e^2}{|\mathbf{r}_i - \mathbf{r}_j|} | \phi_i \phi_j \rangle. \quad (2.16)$$

Until now, we didn't get anything useful. However the original problem was cleverly rewritten in a way, that the minimization of  $E^{\text{KH}}$  produces the so-called Kohn-Sham equations. These are the effective one-particle equations which are Schrödinger-like. Their eigenfunctions are called Kohn-Sham orbitals  $\phi_i(\mathbf{r})$  which depend on the particle density  $\rho(\mathbf{r}) = \sum_i |\phi_i(\mathbf{r})|^2$ .

The solution of the Kohn-Sham equation gives rise to the total ground state energy as

$$E_0[\rho_0] = E_{\text{nuc}} + E_{\text{kin}} + E_{\text{H}} + E_{\text{xc}} \quad (2.17)$$

including the potential of the electron-nuclei interaction, the kinetic energy, the Hartree potential and the exchange-correlation functional.

## 2.4.2 Approximations for the exchange-correlation functional

In contrast to the other functionals on the left side in eq. (2.17), the exchange-correlation part is not known exactly, thus one has to think about some approximation schemas. There are different kinds, the simplest one is the local density approximation (LDA) where

$$E_{\text{xc}}^{\text{LDA}}[\rho] = \int \epsilon_{\text{xc}}(\rho(\mathbf{r}))\rho(\mathbf{r})d\mathbf{r} \quad (2.18)$$

with the many-body exchange-correlation energy per electron  $\epsilon_{\text{xc}}(\rho)$  of a uniform gas with density  $\rho(\mathbf{r})$  of interacting electrons.

In this thesis the Perdew-Burke-Ernzerhof (PBE) functional which is a generalized gradient approximation (GGA) has been used. It is a semilocal-density functional, which is not only dependent on the density at a position  $\mathbf{r}$ . This functional is better for big molecules or systems.

It is of the form:

$$E_{\text{xc}}^{\text{PBE}} = \int d^3r \rho(\mathbf{r}) \epsilon_{\text{xc}}^{\text{PBE}}(r_s(\mathbf{r}), s(\mathbf{r}), \zeta(\mathbf{r})) \quad (2.19)$$

where  $r_s$  is the Wigner-Seitz radius,  $\zeta$  is the spin polarization and the reduced density gradient  $s = \frac{|\nabla\rho|}{2k_F\rho}$  with  $k_F = (3\pi^2\rho)^{\frac{1}{3}}$ .

## 2.5 Spin-orbit coupling

This subsection follows the content of [17] appendix 4,5 and 6.

### 2.5.1 Spin-orbit coupling in Schrödinger equation

The spin-orbit interaction is the mutual interaction between a particles spin and its motion. The Dirac-equation for electrons (2.20) explaines why this type of coupling should be included in the Schrödinger equation, or rather the Pauli equation, since we are including the additional spin structure by two spinors:

$$(c\boldsymbol{\alpha} \cdot \mathbf{p} + c^2(\beta - 1) + V) \Psi = \epsilon \Psi \quad (2.20)$$

where  $\Psi$  is a four-dimensional wave function whereas  $\boldsymbol{\alpha}$  and  $\beta$  are the  $4 \times 4$  matrices

$$\boldsymbol{\alpha} = \begin{pmatrix} 0 & \boldsymbol{\sigma} \\ \boldsymbol{\sigma} & 0 \end{pmatrix} \quad \text{and} \quad \beta = \begin{pmatrix} \mathbb{1}_2 & 0 \\ 0 & -\mathbb{1}_2 \end{pmatrix} \quad (2.21)$$

with  $\boldsymbol{\sigma} = (\sigma_x, \sigma_y, \sigma_z)$ :

$$\sigma_x = \begin{pmatrix} 0 & 1 \\ 1 & 0 \end{pmatrix}, \quad \sigma_y = \begin{pmatrix} 0 & -i \\ i & 0 \end{pmatrix}, \quad \sigma_z = \begin{pmatrix} 1 & 0 \\ 0 & -1 \end{pmatrix}. \quad (2.22)$$

which are the Pauli matrices. The term  $\boldsymbol{\alpha} \cdot \mathbf{p}$  explicitly shows the coupling of spin and momentum, since it includes a momentum operator, which acts on the orbital wave function, and the matrix  $\boldsymbol{\alpha}$ , which is acting on the spin degrees of freedom. It is essential to solve the equation which includes the coupling of all  $\Psi$  components.

Fortunately in condensed matter systems it is possible to expand eq.(2.20) in terms of  $\frac{v}{c}$  and get a simpler non-relativistic equation which is still quite precise. In order to do so, we separate  $\Psi$  into two components, the 'larger'  $\Psi_L$ , which dominates for the non-relativistic limit, has positive energies and therefore represents the electron and the 'smaller'  $\Psi_S$  component with negative energies and which represents a positron.

$$\Psi = \begin{pmatrix} \Psi_L \\ \Psi_S \end{pmatrix} \quad (2.23)$$

Substitution into Dirac equation (2.20):

$$\left[ c \begin{pmatrix} 0 & \boldsymbol{\sigma} \\ \boldsymbol{\sigma} & 0 \end{pmatrix} \cdot \mathbf{p} + c^2 \left( \begin{pmatrix} \mathbb{1}_2 & 0 \\ 0 & \mathbb{1}_2 \end{pmatrix} - 1 \right) + V \right] \begin{pmatrix} \Psi_L \\ \Psi_S \end{pmatrix} = \epsilon \begin{pmatrix} \Psi_L \\ \Psi_S \end{pmatrix} \quad (2.24)$$

$$\Leftrightarrow c \begin{pmatrix} \boldsymbol{\sigma} \cdot \mathbf{p} & \Psi_S \\ \boldsymbol{\sigma} \cdot \mathbf{p} & \Psi_L \end{pmatrix} + c^2 \begin{pmatrix} \Psi_L \\ \Psi_S \end{pmatrix} + (-2c^2 + V) \begin{pmatrix} \Psi_L \\ \Psi_S \end{pmatrix} = \epsilon \begin{pmatrix} \Psi_L \\ \Psi_S \end{pmatrix} \quad (2.25)$$

$$\Leftrightarrow c \begin{pmatrix} \boldsymbol{\sigma} \cdot \mathbf{p} & \Psi_S \\ \boldsymbol{\sigma} \cdot \mathbf{p} & \Psi_L \end{pmatrix} + \begin{pmatrix} V & \Psi_L \\ (-2c^2 + V) & \Psi_S \end{pmatrix} = \epsilon \begin{pmatrix} \Psi_L \\ \Psi_S \end{pmatrix} \quad (2.26)$$

yields two coupled equations

$$(i) \quad c (\boldsymbol{\sigma} \cdot \mathbf{p}) \Psi_S + V \Psi_L = \epsilon \Psi_L$$

$$(ii) \quad c (\boldsymbol{\sigma} \cdot \mathbf{p}) \Psi_L + (-2c^2 + V) \Psi_S = \epsilon \Psi_S$$

Transpose Eq.(ii)

$$((2c^2 - V) + \epsilon) \Psi_S = c (\boldsymbol{\sigma} \cdot \mathbf{p}) \Psi_L \quad (2.27)$$

$$\Leftrightarrow \Psi_S = c \left( \frac{1}{2c^2 - V + \epsilon} \right) (\boldsymbol{\sigma} \cdot \mathbf{p}) \Psi_L \quad (2.28)$$

$$\Leftrightarrow \Psi_S = \frac{1}{2c} \left( 1 + \frac{\epsilon - V}{2c^2} \right)^{-1} (\boldsymbol{\sigma} \cdot \mathbf{p}) \Psi_L, \quad (2.29)$$

then inserting into Eq. (i)

$$c (\boldsymbol{\sigma} \cdot \mathbf{p}) \left[ \frac{1}{2c} \left( 1 + \frac{\epsilon - V}{2c^2} \right)^{-1} \right] (\boldsymbol{\sigma} \cdot \mathbf{p}) \Psi_L + V \Psi_L = \epsilon \Psi_L \quad (2.30)$$

and by finally using  $(\boldsymbol{\sigma} \cdot \mathbf{a})(\boldsymbol{\sigma} \cdot \mathbf{b}) = (\mathbf{a} \cdot \mathbf{b}) + i(\mathbf{a} \times \mathbf{b}) \cdot \boldsymbol{\sigma}$  we obtain

$$\left( \mathbf{p} \frac{c^2}{2c^2 + \epsilon - V} \mathbf{p} + i \mathbf{p} \frac{c^2}{2c^2 + \epsilon - V} \times \mathbf{p} \cdot \boldsymbol{\sigma} + V \right) \Psi_L = \epsilon \Psi_L \quad (2.31)$$

This equation is similar to the Schrödinger equation and is now quadratic in the momentum  $\mathbf{p}$ . For the scalar relativistic case, FHI-aims solves (2.31) without including the second term. This term is corrected in respect to the kinetic energy and is called the

*scalar* relativistic Schrödinger equation. The well-known Schrödinger equation can be recovered by expanding eq. (2.31) to lowest order in  $(\epsilon - V)/2c^2$ . Indeed,

$$\frac{c^2}{2c^2 + \epsilon - V} = \frac{1}{2} \frac{1}{1 + \frac{\epsilon - V}{2c^2}} \quad (2.32)$$

which equals  $\frac{1}{2}$  for the zeroth order. The expansion of the first and second term is the same, but note that the crossproduct of these two identical vectors  $\mathbf{p} \times \mathbf{p}$  is zero. This leads to the non-relativistic Schrödinger equation:

$$\left( \frac{1}{2} \mathbf{p}^2 + V \right) \Psi_L = \epsilon \Psi_L \quad (2.33)$$

Now let us consider the lowest non-trivial order of corrections coming from the second term in (2.31) by using the Taylor series of the geometric series:

$$f(x) = \frac{1}{1+x} \quad (2.34)$$

$$\text{Taylor series to first order: } f(a) + \frac{f'(a)}{1!}(x-a) \quad (2.35)$$

$$\Rightarrow \frac{1}{1+a} + \frac{1}{2} \left( -\frac{1}{(1+a)^2} \right) (x-a) \underset{x=-V/2c^2}{\overset{a=0}{\equiv}} 1 + \frac{V}{2c^2} \quad (2.36)$$

By setting  $\epsilon = 0$  and looking for the non-trivial correction we obtain the spin-orbit interaction term

$$V_{SOC} = \frac{i}{4c^2} \mathbf{p} V \times \mathbf{p} \cdot \boldsymbol{\sigma}. \quad (2.37)$$

Relativistic effects don't need to be considered for structures with light atoms, if the electron is not near the nuclei. But if a structure contains heavy elements, like HgTe, it is necessary since spin-orbit also affects valence electrons.

Finally, we would like to point out that the actual calculation of FHI-aims, is not considered self-consistently but is applied only after the self-consistent cycle of the density has converged.

## 2.5.2 SOC impact on band structure

The splitting behavior of the bands, which will be seen later in the results, is explained as follows.

Beginning with the non-relativistic Schrödinger equation, the eigenstates with angular momentum  $\ell$  and the spin  $s$  can be written as a tensor product of a spatial function and a spin function, the spinor. For certain states, for example the s,p,d, etc. states for spherically symmetric potential, a particular symmetry of an external potential result in a particular banding of eigenvalues and symmetries between eigenvectors.

Adding the scalar-relativistic which brings us to the Schrödinger equation made out of the first part in 2.31 plus the  $V$ , the symmetry of the system doesn't change, but the

Hamiltonian does. That means, that the eigenvalue of single electrons change, but the banding does not.

Turning on the spin-orbit coupling leads to a conservation of the total angular momentum  $j = \ell + s$ , but angular momentum and spin are no longer separately conserved. Consequently, the degeneracy in the spin quantum number might be lifted by the spin-orbit interaction and the bands might split (in some situations, some bands might still present accidental degeneracies) As a consequence, it is possible that the degeneracy in the spin quantum number is been reinforced by the spin-orbit coupling, so that the bands might split up. But note, that sometimes, some bands can still have coincidental degeneracies. If the band splitting is very strong, some bands can even get inverted.

## 3 Results

### 3.1 Input for FHI-aims

All results were obtained by using FHI-aims [2]. The input data are the files control.in and geometry.in. The geometry.in contains the lattice vectors' coordinates and the positions and types of the atom forming the basis. One example for the calculations of the bulk HgTe properties is:

```
# hgte lattice constant 6.685 AA
lattice_vector 0.00000 3.34250 3.34250
lattice_vector 3.34250 0.00000 3.34250
lattice_vector 3.34250 3.34250 0.00000

atom 0.00000 0.00000 0.00000 Te
atom 1.67125 1.67125 1.67125 Hg
```

The control.in contains all physical and computational settings for the calculation. The properties for the atoms also appear in the control.in, specifically the different types of basis sets settings. One can choose between *light*, *tight* and *really tight*, in this thesis we were using the *light* settings. Among the setting one must consider is the exchange-correlation functional, the spin, the numerical settings for the self-consistency cycle convergence and the grid size of the reciprocal lattice. For example see what we used for the bulk HgTe calculations:

```
# Physical settings
xc pbe                      # methode to be used, here pbe
spin none                    # spin treatment
relativistic atomic_zora scalar # include relativistic effects
default_initial_moment 0      # initial spin for the atoms
#
# SCF convergence          # convergence criteria of self convergence cycle
sc_accuracy_rho 1E-4        # of change of density
sc_accuracy_eev 1E-2         # of sum of orbital eigenvalues
sc_accuracy_etot 1E-5        # total energy between two consecutive cycles
sc_iter_limit 100            # maximum of iterations
#
# k_grid settings
k_grid 8 8 8                 # k_x k_y k_z for the integration in k-space
```

Spin none means that we deal with closed-shell calculations, in other words, the valence shell is regarded as filled [3]. The relativistic effects had to be taken into account since Hg and Te are both heavy elements and spin-orbit coupling, which is at the heart of the properties of topological insulators, can be considered as a low energy relativistic effect.

### 3.2 The lattice constant and the k-grid

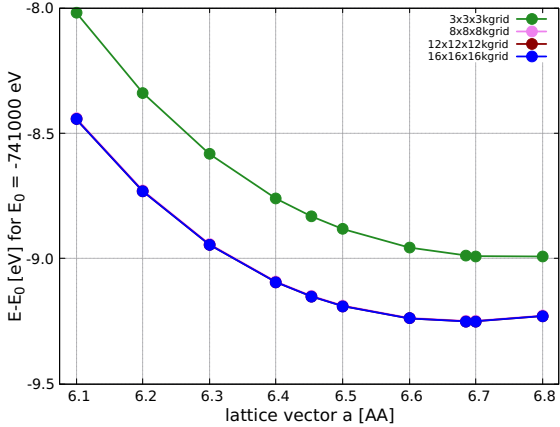


**Figure 8.** Lattice constant  $a$  with respect to the total energy, calculated with four different k-grids. Lines for k-grids 8x8x8, 12x12x12 and 16x16x16 are overlaid.

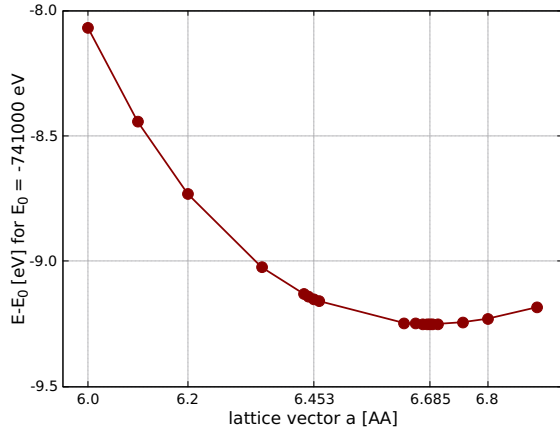


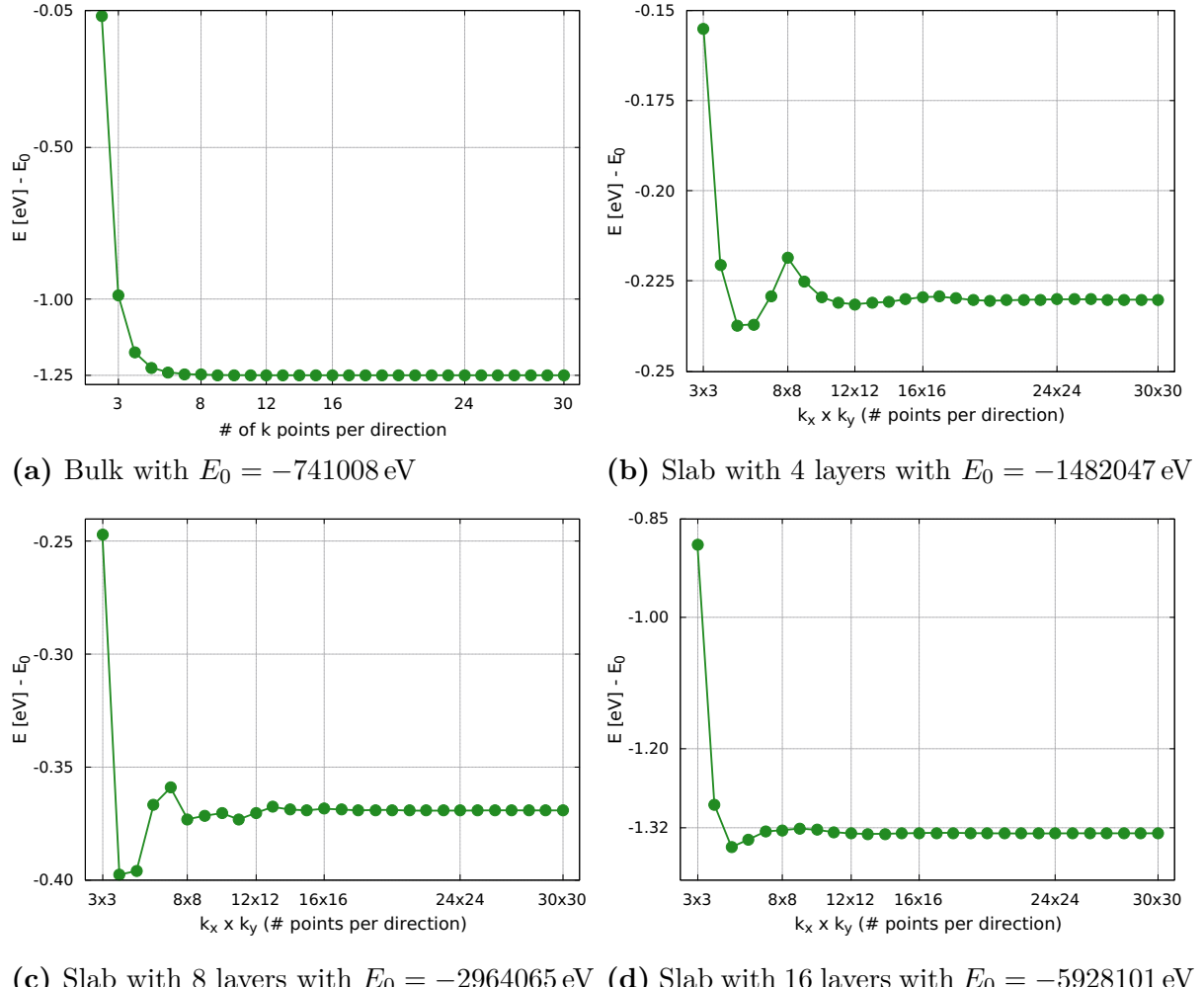
**Figure 9.** Lattice constant  $a$  with respect to the total energy. The lowest energy was found for 6.685 Angström.

First of all the lattice constant  $a$  with the lowest total energy in the HgTe bulk must be determined, since the energetically most stable constitution of a crystal structure is given by the smallest total system energy respective to the lattice constant. Both the bulk and the slab calculations must have the right values for the the k-grid density in order to make calcutions faster and less computationally expensive.

In figure 8 one can see the result for lattice vector  $a$  in Angström with respect to the total energy of the bulk, with different k-grids. It is clear, that 3x3x3 gives no representative results.

After carefully looking at the results of the energy convergence tests, the lattice constant was determined by using a higher k-grid than 8x8x8 to be sure about the convergence of the calculations. The result of the final step to determine the best theoretical value of the lattice constant for our crystal structure can be seen in figure 9. As one can see, the best results were obtained for a lattice constant of 6.685 Angstrom.

It is this lattice constant, that was used for executing a detailed k-grid study. The results of this study is shown in figure 10 where additionally the results for the slabs with 4, 8 and 16 layers are illustrated. It is not surprising that the most economic values of the k-grids for the slabs are virtually the same as for the bulk namely around 12x12x12. But since for higher k-grids the band structure curve becomes smoother, we used 24x24x24 in order to get smooth results. Note that although the CPU time therefore increases, this is not significant for the calculations of the systems regarded in this thesis.



**(c)** Slab with 8 layers with  $E_0 = -2964065$  eV **(d)** Slab with 16 layers with  $E_0 = -5928101$  eV

**Figure 10.** Total energy  $E[\text{eV}] - E_0$  (with  $E_0$  the energy offset) as a function of  $k$ -grid spacing.

### 3.3 The bulk band structure in the first 3D Brillouin zone

The calculations for the bulk band structure are made in the 3D Brillouin zone. For the calculation of the bulk band structure, we use the following path (like in [17] p.12)

$$L \rightarrow \Gamma \rightarrow X \rightarrow W \rightarrow K \quad (3.1)$$

Those symmetry points are illustrated in figure 6 in the theory part. The k-grid and the command used in order to extract the band structure output from FHI-aims is defined in the control.in file as

```
# k_grid settings
k_grid 24 24 24
#
# output band structure
output band 0.5 0.5 0.5 0.0 0.0 0.0 21 L Gamma
output band 0.0 0.0 0.0 0.0 0.5 0.5 21 Gamma X
output band 0.0 0.5 0.5 0.25 0.5 0.75 21 X W
output band 0.25 0.5 0.75 0.375 0.375 0.75 21 W K
```

The geometry.in input is the same as the one mentioned in subsection 3.1.

The outcome of the band structure calculations is shown in figure 11, where the green lines indicate the band structure without spin-orbit coupling (SOC) and the blue lines are the calculations with SOC.

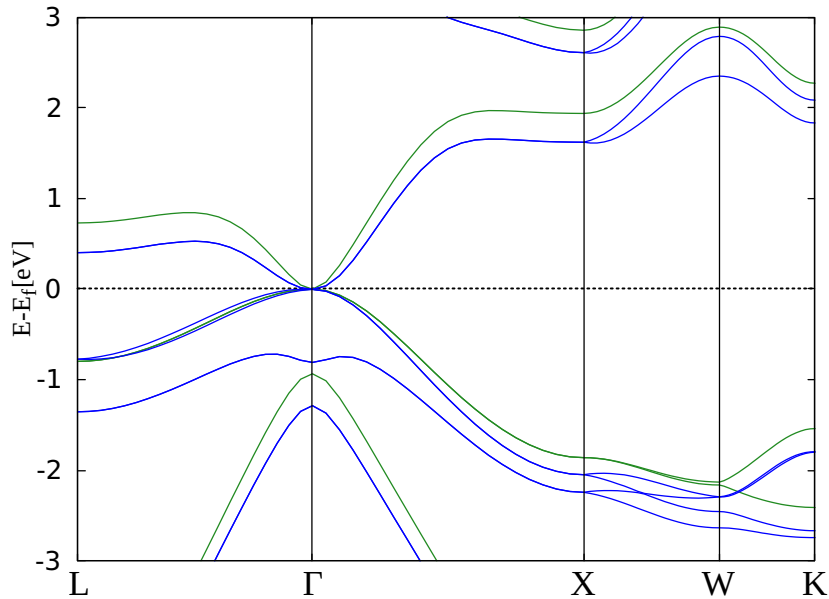


**Figure 11.** Band structure of bulk HgTe in the first 3D Brillouin zone. The green lines are the band structure without spin-orbit coupling, and the blue ones include spin-orbit coupling. The Fermi level is indicated by the dashed line.

### 3.4 Projected bulk band structure

As mentioned before, the band structure of the bulk is calculated along the high symmetry points in the 3D Brillouin zone, see figure 6. But to compare the bulk band structure with the surface band structure from the slab, the bulk must be analyzed by using the so-called projected bulk band structure (PBBS). By superimposing the plots of the slab's band structure with the PBBS, the bulk states can be distinguished from the surface states.

The periodic boundary conditions are applied in all directions when we get the band structure for the bulk. As we mentioned in subsection 2.3.3, this is not applicable when we perform the calculations for the surface band structure in the supercell approach for an isolated slab. The slab band structure cannot be calculated like the bulk band structure, because for the surface the translation symmetry is broken. Thus we have to find an other solution how to compare the information about those two systems. At first it must be ensured that the orientation is the same, then we perform band structure calculations for different  $k_z$  values of the bulk. In other words, we make 2D slices of the first 3D Brillouin zones of the bulk such that  $k_z$  is perpendicular to them. Once these calculations are done, we put them all together in an ensemble which then represents the PBBS in that direction. As soon as we have the PBBS, we can compare it with the band structure of the slabs in the (001) growing plane. For this purpose, we calculate the band structure by following the path through the high symmetry points in the 2D Brillouin zone:

$$\bar{J} \rightarrow \bar{\Gamma} \rightarrow \bar{K} \rightarrow \bar{J} \quad (3.2)$$

The band structure for the slabs will look different for different terminations of the surface while we follow the same path along the high symmetry points. The lines which lie in the gap are energy bands corresponding to surface states, which can be trivial surface states or topological surfaces states. In practical terms, we proceed by exchanging the  $k_z$  in output instructions in the control.in file by different values. In sufficient small steps  $k_z$  goes from  $k_z = 0$  to  $k_z = k_{z,\max}$ , with  $k_{z,\max} = \frac{\pi}{a}$  where  $a$  is the lattice constant. This value of the  $k_z$  corresponds to the edge of the first BZ.

Regarding the calculations of the band structure for the slab, we need to take into account that since we have a 2D Brillouin zone, the path along the Brillouin zone through the high symmetry points must be in the same plane. In our case, since we are interested in the (001) direction, we need to set  $k_z = 0$  in order to get the energy bands.

Here is an example of how to plot one slice of the Brillouin zone in the PBBS, where the slice is at  $k_z = 1/40 * k_{z,\max}$ :

```
# output band structure
output band 0.5  0.0  0.01175  0.0  0.0  0.01175  80  J      Gamma
output band 0.0  0.0  0.01175  0.5  0.5  0.01175  80  Gamma K
output band 0.5  0.5  0.01175  0.5  0.0  0.01175  80  K      J
```

The three numbers after the term `output band` are indicating the point in the path

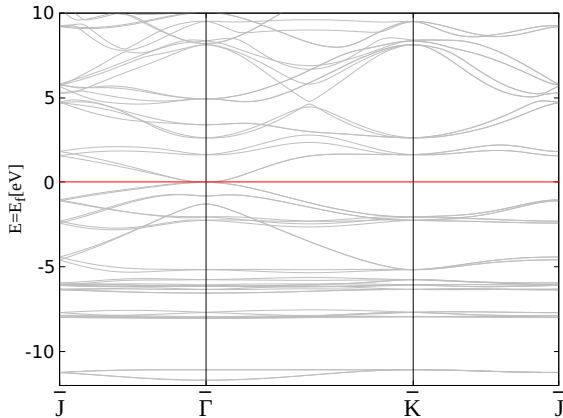
where one starts the calculation for the energy band in the reciprocal space, while the fourth to the sixth number are the coordinates for the point of the path where one finishes the energy band calculation in the reciprocal space. The last number: 80 is the number of points which divides that segment of the path. The sharpness of the energy bands depends on the k-grid density and the number of points you take in each segment. The letters at the end of the line are labeling the first point and the final point of the calculation through the path.

As final comment, remark that we choose 80 as parameter to compute the energy bands along a segment after 21 points for the calculations of figure 11 led to bands that were not smooth at some point.

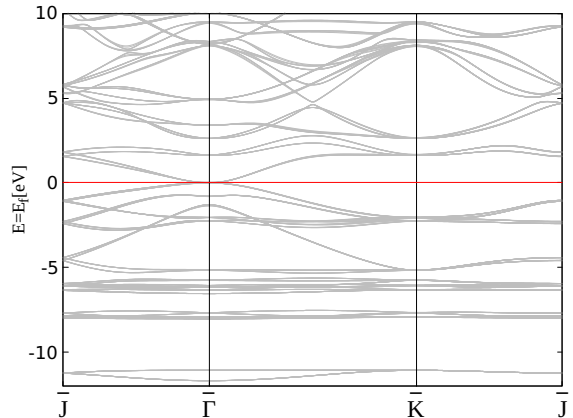
As we explained at the beginning of this subsection, once the band structures are calculated for several values of  $k_z$ , we then have to put all bands in a single plot in order to visualize the PBBS. This situation can be seen in figure 12.

In the figures 13, 14 and 15 we represent the plots of the band structures for Te-Hg termination for 4, 8 and 16 layers. In these figures, we can also see the band structure calculation for slabs which have symmetric Te-Te and Hg-Hg terminations, as well as the band energies corresponding to the different terminations with or without passivation by hydrogens at one surface.

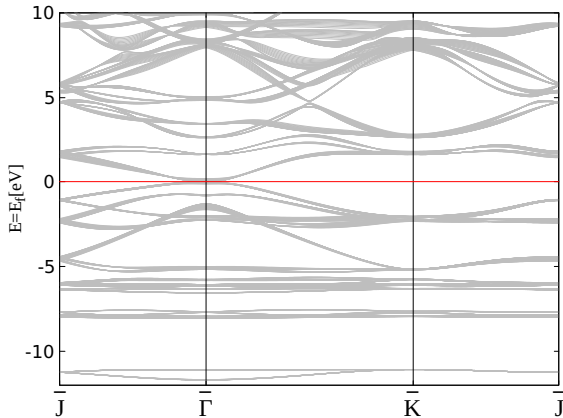
The grey part is the PBBS part, the blue lines are the band structure of the slabs and the red line marks the Fermi level.



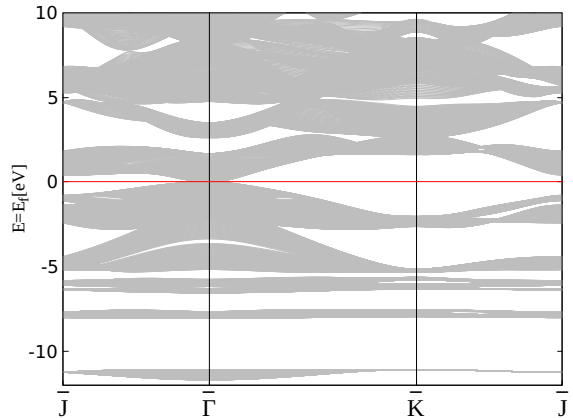
(a) PBBS for  $k_z$  is equal to zero.



(b) Ensemble for PBBS for  $k_z$  having values from 0 to  $1/10 \cdot k_{z,\text{max}}$

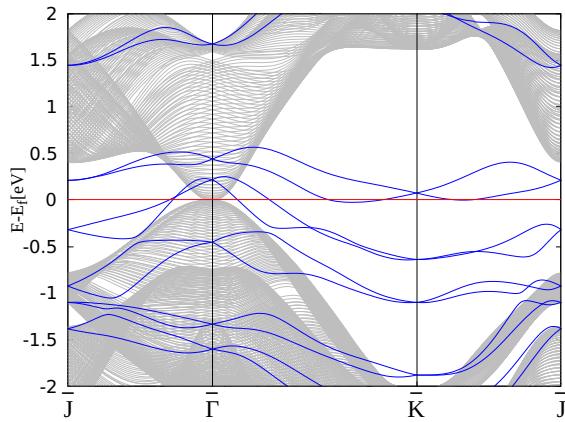


(c) Ensemble for PBBS for  $k_z$  having values from 0 to  $1/4 \cdot k_{z,\text{max}}$

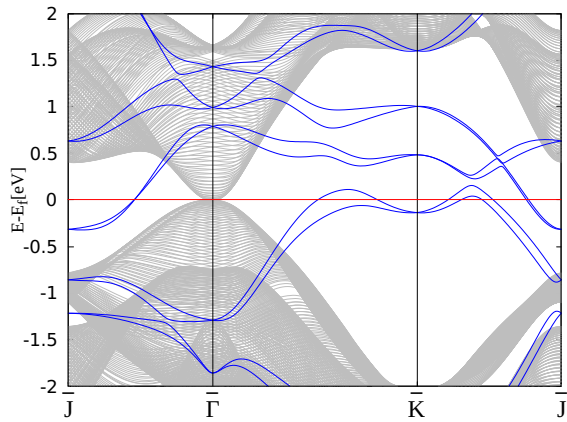


(d) Whole PBBS for all the values of  $k_z$  going from 0 to  $k_{z,\text{max}}$

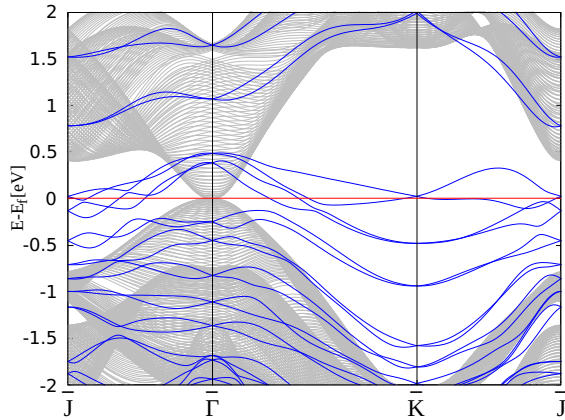
**Figure 12.** Generation of projected bulk band structure of HgTe



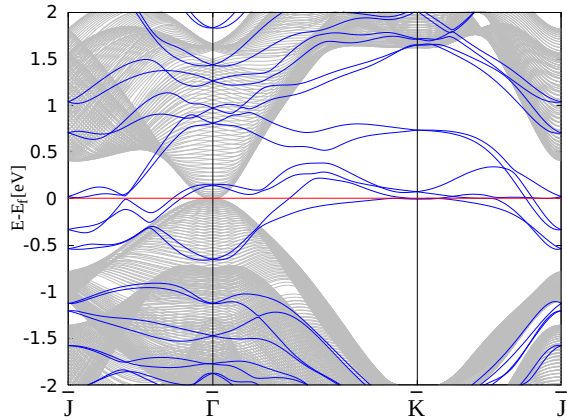
(a) 4 layers without hydrogens passivating the Te termination



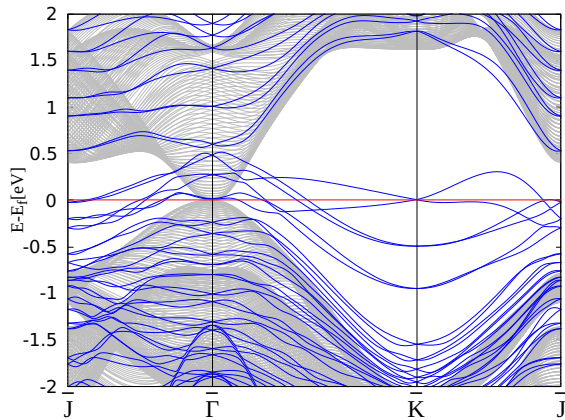
(b) 4 layers with hydrogens on the bottom passivating the Te surface terminations



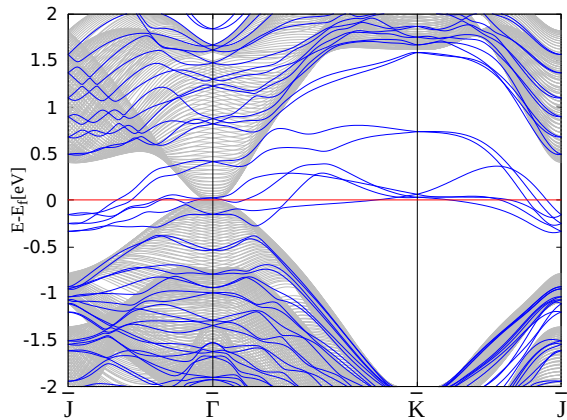
(c) 8 layers without hydrogens passivating the Te termination



(d) 8 layers with hydrogens on the bottom passivating the Te surface terminations

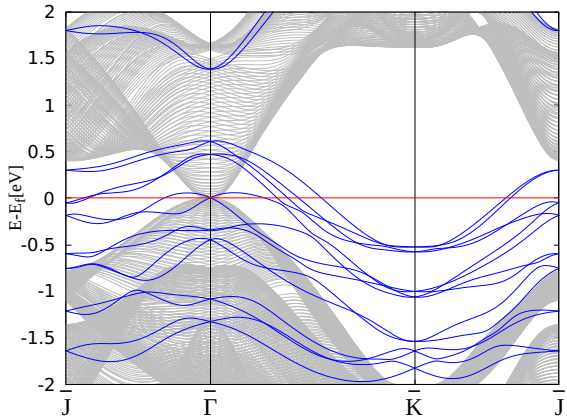


(e) 16 layers without hydrogens passivating the Te termination

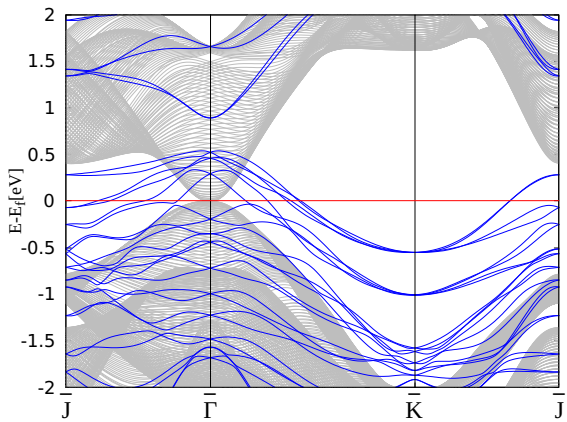


(f) 16 layers with hydrogens on the bottom passivating the Te surface terminations

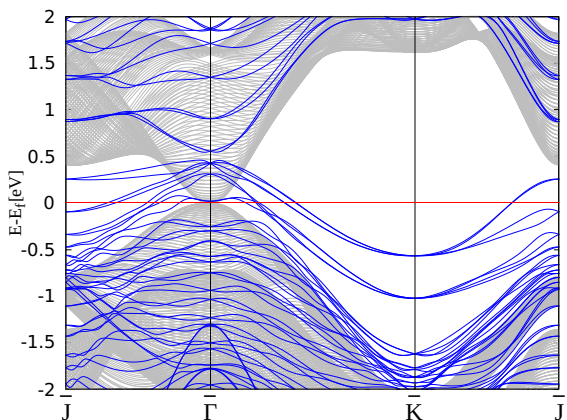
**Figure 13.** PBBS and surface band structure for Te-Hg terminations



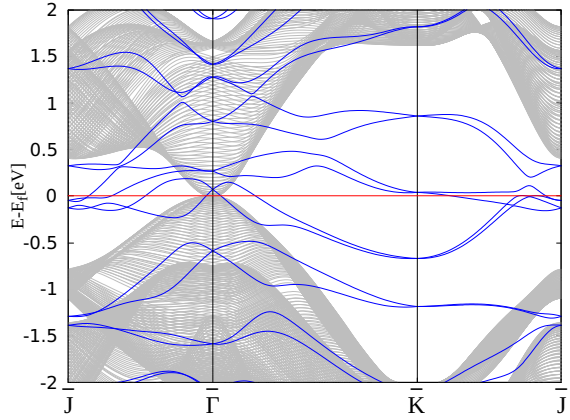
(a) 5 layers without hydrogens passivating one of the surfaces



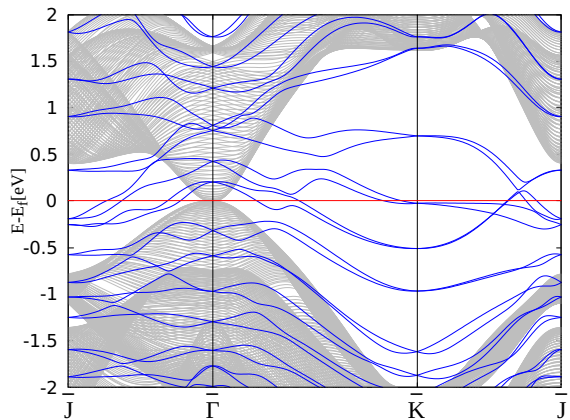
(c) 9 layers without hydrogens passivating one of the surfaces



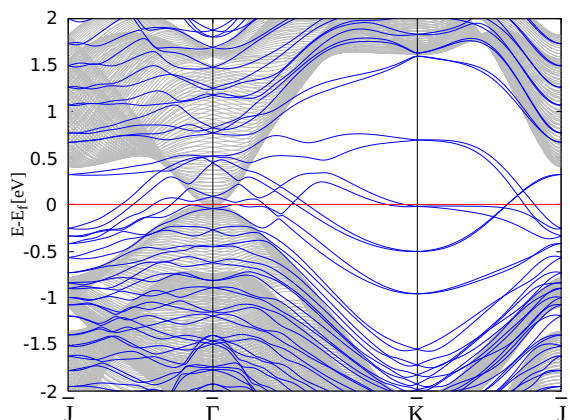
(e) 17 layers without hydrogens passivating one of the surfaces



(b) 5 layers with hydrogens on the bottom passivating one of the Te surfaces terminations

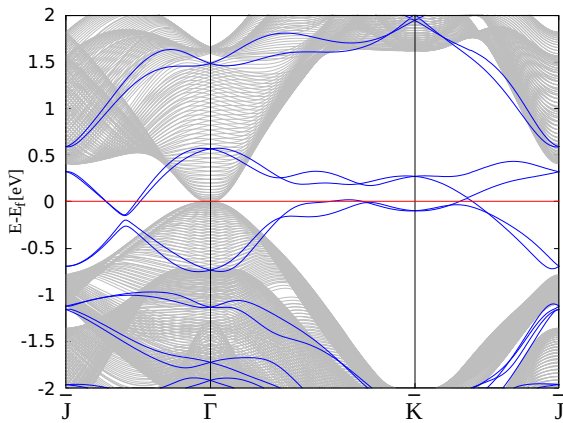


(d) 9 layers with hydrogens on the bottom passivating one of the Te surfaces terminations

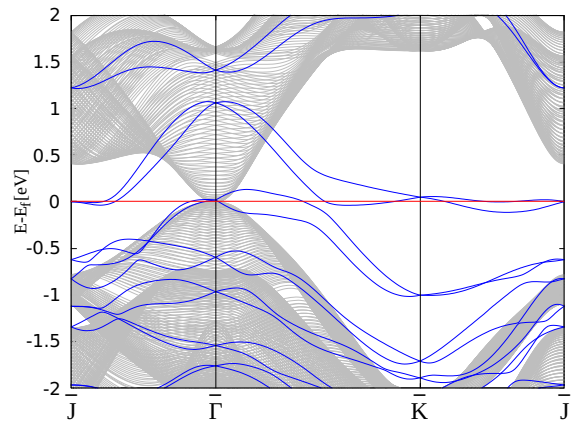


(f) 17 layers with hydrogens on the bottom passivating one of the Te surfaces terminations

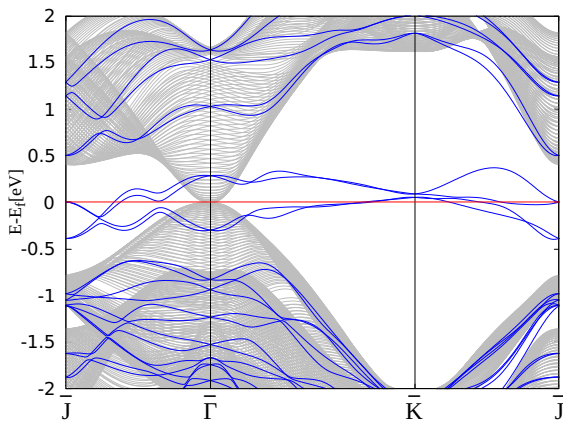
**Figure 14.** PBBS and surface band structure for symmetric Te termination on both surfaces of the slab



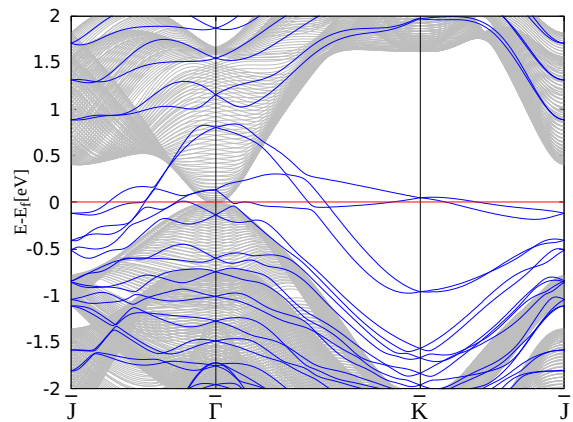
(a) 5 layers without hydrogens passivating one of the surfaces



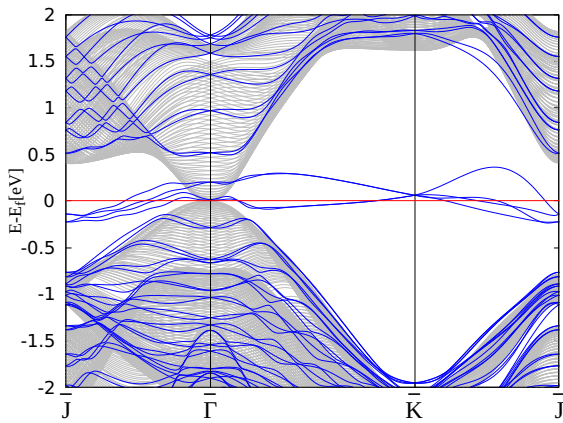
(b) 5 layers with hydrogens on the bottom passivating one of the Hg surface terminations



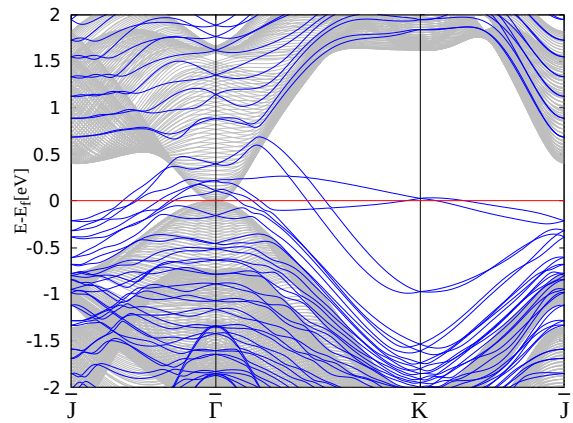
(c) 9 layers without hydrogens passivating one of the surfaces



(d) 9 layers with hydrogens on the bottom passivating one of the Hg surface terminations



(e) 17 layers without hydrogens passivating one of the surfaces



(f) 17 layers with hydrogens on the bottom passivating one of the Hg surface terminations

**Figure 15.** PBBS and surface band structure for symmetric Hg termination on both surfaces of the slab

## 4 Interpretation of the results

### 4.1 k-grid study

At the beginning of the calculations we demonstrated, that for the evaluation of the bulk HgTe the most economic k-grid setting for dividing the reciprocal space is 8x8x8. Note that for higher k-grids, which means smaller steps of discretization more CPU time is required but would not harm the calculations.

The same study was performed on different slab thicknesses. Those results showed that the total energy as a function of k-grid steps was oscillating before it finally converged like the study did for the bulk. This oscillation has its origins in the broken translation symmetry in the direction perpendicular to the surface. The thinner the slabs is, the more apparent this side effect becomes because it affects more atoms per unit cell.

### 4.2 Lattice constant study

In subsection 3.2 we performed the study of the lattice constant for bulk HgTe. We showed that the minimum value of energy is reached at the lattice constant  $a = 6.685 \text{ \AA}$ . For comparison the experimental value at room temperature is  $a = 6.46152 \text{ \AA}$  and for LDA calculations, which was explained in subsection 2.4.2, the value is  $a = 6.346 \text{ \AA}$  (data from [15]).

### 4.3 Bulk band structure

We calculated the bulk band structure for HgTe with and without spin-orbit coupling for regarding the impact spin-orbit interactions have on mercury telluride.

It seems that, because HgTe is made out of heavy elements, the calculations in which spin-orbit coupling is included are giving physically meaningful results. Due to the spin-orbit interaction the original spin-degenerated bands are splitting up, as shown in figure 11. It is well known that for zinc-blende semiconductors the band splitting leads to a heavy hole band, a light gap band and a double degenerated conduction band near the  $\Gamma$  point [5] which is reproduced by our calculations.

### 4.4 PBBS and the band structure of the slabs

In the main part we made the projected bulk band structure which represents the energy dispersion relation for electrons in HgTe. Therefore we calculated the dispersion relation for different  $k_z$  in order to study slices of the first 3D Brillouin zone. In our case we concentrate on the (001) direction. As mentioned before in subsection 2.3.3, this is the growing direction of the slabs on which we want to analyze the potentially topological surface states. The plot for the projected bulk band structure in  $k_z$  direction is shown in figure 12. The grey area correlates to the energy values an electron can adopt if one is looking on the bulk band structure from  $k_z$  direction. Note that this only gives information about the bulk.

Therefore we calculated the band structures for the slabs with different thickness and terminations at the surfaces. Note that the Fermi energy was set to zero and that we only regarded ideal surfaces. Of course we see the band splitting caused by the spin-orbit interaction, seen in the bulk band structure, also in the slab surface bands.

After that we superimposed the band structures of the slabs and the PBBS and noticed that the slab bands appear in the white area of the PBBS as well as in the grey area which belongs to the bulk. The bands of the slabs, which are in the grey region, are bulk energy bands while the slab bands which cross the white area, the band gap of the bulk, are the surface states. The latter can be either trivial or topological surface states, which we can distinguish by looking from where those bands come from and where they go to. A band can only represent a topological surface state if the band comes from the valence/conduction band and goes to the conduction/valence band. Additionally one can count how many times the dispersion line crosses through the Fermi level. If the number of crossings is odd, then this energy band is a topological surface state [4].

By looking at figure 13, 14 and 15 we notice that slab band structure is very sensitive under variation of thickness and terminations. It stands out, that the number of bands rises as the slabs are becoming thicker. In the plots for 16 and 17 layers we find energy bands which lie entirely within the PBBS. These represent the bulk states. On the contrary the bands lying completely in the band gap are the surface states which can be seen clearly in figure 13, 14 and 15 in (e) and (f).

Since we turn our attention particularly to the evolution of the topological surface states, we observe that the structure of the dispersion relation differs much for different surface terminations. Regarding the slabs with one surface passivated by hydrogens, then we see that the energy bands corresponding to the surface states are shifted away from the Fermi level [11]. In the plots for clear terminations one can observe possible candidates for a Dirac cone.

By counting all crossings of the dispersion energy through the Fermi level we only discover trivial surface states. This is provoked by the dangling bonds at the crystal's surface. In order to see topological surface states we could use just strained HgTe like in [5] or use the c(2x2)-type reconstruction like in [11]. In the latter case they studied Te-terminated slabs and found Dirac cones at the  $\Gamma$  point once strain was applied and semi-infinite slabs were studied. For symmetric Hg-terminations they found Dirac cones at  $\bar{K}$  and  $\bar{J}$  in (001) direction in case of clean surfaces. The hydrogens effects the isotropic Dirac cone in a way that they become anisotropic cones.

The reconstruction of the surfaces, the simulation of strains and the simulation of semi-infinite surfaces is beyond this bachelor thesis.

## 5 Conclusion

In this thesis we performed ab-initio calculations for the dispersion energy in case of thin HgTe films with different thicknesses and terminations. These slabs were regarded as grown in the crystallographic (001) direction.

We compared the bulk band structures in which we did or did not include the spin-orbit coupling and showed that band splitting can be observed by including the spin-orbit interactions. The superimposing of the slab energy bands and the projected bulk band structure in (001) direction allowed us to identify the surface states and additionally to discuss the topological character of HgTe in that direction. After analyzing the surface band structure we discovered that, because of the dangling bonds at the surface, all of them are trivial surface states.

Finally we pointed out that for strained HgTe or for surface reconstruction of Hg- and Te-terminations the observation of topological surface states is possible.

## References

- [1] URL: [https://en.wikipedia.org/wiki/Topological\\_insulator#/media/File:Topological\\_insulator\\_band\\_structure.svg](https://en.wikipedia.org/wiki/Topological_insulator#/media/File:Topological_insulator_band_structure.svg).
- [2] URL: <https://aimsclub.fhi-berlin.mpg.de/>.
- [3] URL: [https://en.wikipedia.org/wiki/Open\\_shell#cite\\_note-3](https://en.wikipedia.org/wiki/Open_shell#cite_note-3).
- [4] A. Bansil et al. In: *Rev. Mod. Phys.* 88.021004 (2016).
- [5] S.-C. Wu et al. In: *epljournal* 107.57006 (2014). DOI: 10.1209/0295-5075/107/57006.
- [6] W. Kohn et al. URL: [http://www.nobelprize.org/nobel\\_prizes/chemistry/laureates/1998/kohn-lecture.pdf](http://www.nobelprize.org/nobel_prizes/chemistry/laureates/1998/kohn-lecture.pdf).
- [7] B.A. Bernevig and S.C. Zhang. In: *Physical Review Letters* 96.106802 (2006).
- [8] P. Ballet X. Baudry R. B. G. Kramer L. Lévy C. Bouvier T. Meunier. In: (). URL: <https://arxiv.org/abs/1112.2092v1>.
- [9] E. J. Mele C. L. Kane. In: *Phys. Rev. Lett.* 95.226801 (2005).
- [10] E. J. Mele C. L. Kane. In: *Phys. Rev. Lett.* 95.146802 (2005).
- [11] M. Richter J. v. d. Brink F. Virot R. Hayn. In: *Phys. Rev. Letters* 111.146803 (2013).
- [12] G. P. Parravicini G. Grossos. *Solid State Physics*. academic press, 2003.
- [13] Ch. Kittel. *Introduction to Solid State Physics*. 8th ed. Wiley.
- [14] D. W. Knebl. MA thesis. Karl-Franzens-Universität Graz, 2013.
- [15] Landolt-Börnstein. “Semiconductors”. In: *Numerical Data and Functional Relationships in Science and Technology*. Vol. 44. Springer, p. 212.
- [16] Yu. Mastrikov Yu.N. Shunin P.W.M. Jacobs Yu.F. Zhukovskii. In: *Computer Modelling & New Technologies* 6.1 (2002), pp. 7–28.
- [17] Lydia Nemec Björn Bieniek Björn Lange Sebastian Kokott Franz Knuth and William Huh. *Tutorial II: Periodic systems Manuscript for Exercise Problems*. URL: [http://th.fhi-berlin.mpg.de/sitesub/meetings/dft-workshop-2016/uploads/Meeting/Tutorial\\_2\\_2016.pdf](http://th.fhi-berlin.mpg.de/sitesub/meetings/dft-workshop-2016/uploads/Meeting/Tutorial_2_2016.pdf).
- [18] David Singh Z. W. Lu and Henry Krakauer. In: *PhysRev B* 39.10154 (1989).